Volume 40
Number 4
April 2025
Pages 923–1124

JAAS

Journal of Analytical Atomic Spectrometry

rsc.li/jaas

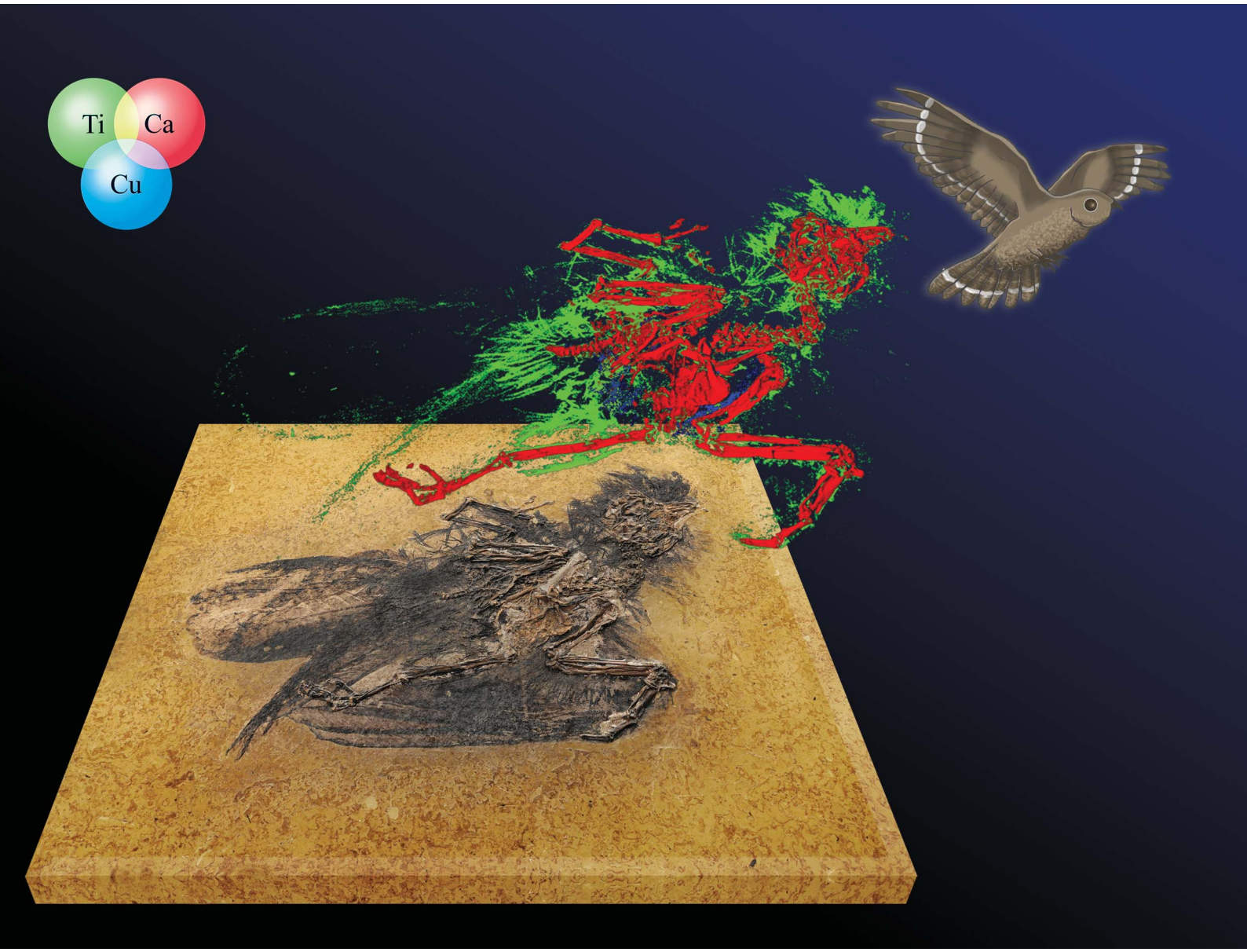

ISSN 0267-9477

PAPER

Marco Colombo, Valentina Rossi *et al.*
Application of mobile-macroscale scanning X-ray fluorescence (mobile-MA-XRF) imaging in paleontology: analyses of vertebrate fossil specimens from Messel conserved in different solid and liquid media

ROYAL SOCIETY OF CHEMISTRY

JAAS

PAPER

View Article Online
View Journal | View Issue

Cite this: *J. Anal. At. Spectrom.*, 2025, 40, 989

Application of mobile-macroscale scanning X-ray fluorescence (mobile-MA-XRF) imaging in paleontology: analyses of vertebrate fossil specimens from Messel conserved in different solid and liquid media†

Marco Colombo, *[a] Thomas Lehmann, [b] Wolfgang Ensinger [a] and Valentina Rossi *[cd]

Cutting-edge analytical instrumentation is increasingly being developed and applied to the analysis of fossils. X-ray fluorescence (XRF) imaging spectroscopy is a powerful tool to resolve the elemental chemistry of fossil specimens. Most of the XRF application to study fossils is carried out at dedicated synchrotron radiation XRF beamlines. Recent studies used laboratory scanners, *i.e.* stationary instruments with a measurement chamber or mobile ones to tackle paleontological questions. The application of these new XRF systems on fossils is still relatively limited and clear protocols for the acquisition and processing of the XRF data are currently lacking. Here, we present the use of mobile-macroscale scanning XRF (mobile-MA-XRF) imaging for the *in situ* analyses of the elemental chemistry of fossil vertebrates from the Messel biota (~48 Ma, Eocene), including amphibians, reptiles, mammals and birds. We investigate the usefulness of mobile-MA-XRF to detect tissue-specific elemental signatures in fossils preserved in solid resin, liquid glycerin and water. We found remarkable tissue-specific chemical signatures preserved in almost all specimens analyzed. Hair and feathers are associated with S and Ti, abdominal tissues with Cu and Zn and stomach contents, *e.g.*, seeds, are associated with Ni, Cu, and Zn. We provide a detailed protocol for acquisition and processing of MA-XRF data and a critical discussion of the application of this approach to paleontological research. Our work sets the foundation for applying MA-XRF to the analyses of those fossils that cannot be measured at synchrotron facilities and/or with stationary laboratory scanners due to their dimensions, weights and conservation mode.

Received 29th August 2024
Accepted 17th February 2025

DOI: 10.1039/d4ja00310a

rsc.li/jaas

1. Introduction

Paleontology is a multidisciplinary analytical field that studies ancient organisms by developing and applying modern advanced technology to analyze fossils, both at the physical and chemical levels.[1–4] Fossils preserving non-biomineralized tissues, *i.e.* soft tissues (*e.g.*, skin, eyespot and various internal organs) and in particular those preserved as carbonaceous films (organic preservation[5]) are of great importance for the research on the preservation of biomolecules, such as melanins,[6–9] keratins[10,11] and other biomolecules.[12–14] These fossils are usually analyzed using a range of analytical methods, encompassing scanning electron microscopy (SEM) and transmission electron microscopy (TEM), gas chromatography-mass spectrometry (GC-MS), Fourier-transform infrared (FTIR) spectroscopy, Raman spectroscopy, synchrotron radiation macro-X-ray fluorescence (SR-MA-XRF) spectroscopy, and X-ray absorption (XAS) spectroscopy.

In the last decade, XRF analyses have proven to be a powerful method to investigate the spatial distribution of key elements in organically preserved melanosome-rich soft tissues[7,15–18] and skeletal elements in fossil vertebrates,[19] to elucidate specific aspects of the taphonomic history[20,21] and biology of extinct animals. These works were possible through the advanced technology at synchrotron beamlines. Here, the tunable energy of the synchrotron permits to singly collect the XRF signals from selected elements of interest.[22] SR-MA-XRF is performed at high spatial resolution and speed, as well as with a high sensitivity for trace elements and signal-to-noise ratio (as the scattering background can be minimized and the incident energy can be

[a]*Technical University of Darmstadt, Department of Materials- and Geosciences, Institute of Materials Science, Material Analysis Division, Peter-Grünberg-Str. 2, 64287 Darmstadt, Germany. E-mail: colombo@ma.tu-darmstadt.de*

[b]*Senckenberg Research Institute and Natural History Museum Frankfurt, Senckenberganlage 25, 60325 Frankfurt am Main, Germany*

[c]*School of Biological, Earth and Environmental Sciences, University College Cork, T23 N73K Cork, Ireland. E-mail: valentina.rossi@ucc.ie*

[d]*Museum of Nature South Tyrol, via Bottai 1, 39100 Bolzano, Italy*

† Electronic supplementary information (ESI) available. See DOI: https://doi.org/10.1039/d4ja00310a

optimized).[23] The high brightness of synchrotron radiation provides small, intense, and collimated beams with long focal lengths. This is particularly advantageous for the XRF imaging of fossil specimens with non-flat surfaces, as it assures they are in focus during scanning.[22] Moreover, XAS analysis can be performed as part of the same synchrotron experiment, and UV-visible monitoring systems able to alert for real-time changes in the sample during a measurement are also available at some synchrotron beamlines.[23,24] SR-MA-XRF can reach maximal imaging ranges of 100 × 60 cm^2 and a total load capacity of up to 25 kg (sample environment and sample).[23] Access to SR-MA-XRF facilities is possible *via* competitive beamtime applications, which, if successful, give to the users a relatively limited analytical time.[25] In addition, only a few synchrotron instruments are optimized for macroscale XRF imaging – *e.g.*, in terms of space or sample environments to allow the movement of large objects,[23,24] posing accessibility limitations to widespread application of SR-MA-XRF to study fossils. In recent years, the technological developments in optics fabrication and detection systems have resulted in new X-ray instrumentation. Notable examples include the development of (i) stationary laboratory scanners (benchtop μ-XRF), and (ii) mobile laboratory scanners for macroscale scanning XRF (mobile-MA-XRF). Recently, their application was expanded to paleontological questions.[26–29] For example, in one of these works, benchtop μ-XRF was used to determine the degree of preservation of sampled fossilized hard tissues (*i.e.*, teeth and bones).[26] However, benchtop μ-XRF spectrometers are limited in the maximum measurable sample size, which in general is dictated by the chamber size and the sample positioning device. The benchtop scanners that were used to study fossils have maximal imaging ranges of 19 × 16 cm^2 and maximum weight load of 7 kg.[30,31] Additionally, the total weight (∼130 kg) of those benchtop instruments and the absence of wheels make their transport difficult. On the contrary, mobile-MA-XRF instruments are characterized by an open-beam set-up, which gives the possibility to scan macroscopic samples (up to several square meters in size),[32] *in situ* (the instrument can be brought to the sample),[29] and with a high spatial resolution (in the 10 to 500 μm range).[23] Recently, mobile-MA-XRF was applied to analyze the elemental chemistry of soft and hard tissues in a dinosaur.[29] One major advantage of the instrument employed is the possibility to use it either vertically (*i.e.*, the specimen can be left on the display wall or case) or horizontally (*i.e.*, the specimen is placed on a table). Further, the variable beam spot size enables overview and detailed XRF scans with an image resolution on the order of 0.5 mm and 100 μm, respectively.[32] Since the first-time use of SR-MA-XRF for the visualization of a hidden painting by Vincent van Gogh[33] and the development of the first mobile scanners for the *in situ* investigation of historical paintings a few years later,[34–37] mobile-MA-XRF has been increasingly used to study artworks. With separate comprehensive elemental distribution images from the entire paint surface, the technique makes it possible to characterize a painting's surface and subsurface layers.[38–40] This offers an insight into a painting's creation process and the *modus operandi* of artists. Moreover, since its development, the technique contributed to elucidate historical, theoretical and conservation related questions about art.[41–46] Other cultural heritage objects, such as stained glass windows,[47] illuminated manuscripts[48–50] and artistic drawings[51,52] can also be examined by means of mobile-MA-XRF. The use of mobile-MA-XRF to investigate the elemental chemistry of large fossils is still limited. Our capacity to extract meaningful information about the taphonomy and biology of fossils is challenged by a general lack of rigorous protocols for data processing to reliably use benchtop μ-XRF scanners and mobile-MA-XRF scanners to answer paleontological questions.

Here we used mobile-MA-XRF to analyze the elemental chemistry of diverse vertebrate fossil specimens from the Lagerstätte of Messel (*ca.* 48 Ma, Eocene) (see ESI, Fig. S1†), including all major classes of tetrapods (*i.e.*, amphibians, reptiles, mammals and birds) preserved in different media: solid epoxy resin (*i.e.*, fossils prepared *via* the resin transfer method), glycerine (liquid medium) and water. The Konservat-Lagerstätte of Messel (Eocene, *ca.* 48 Ma) is a UNESCO World Heritage Site[53] renowned worldwide for the exceptional preservation of its fossils, including both animals and plants. In particular, fossil vertebrates from Messel are known to preserve melanosome-rich soft tissues,[7,54] such as skin, fur, plumage, eyespots and internal organs. Some of these fossils are large (>1 m in length) and fragile (*i.e.*, bones can be easily scuffed by metallic objects). Small specimens are often conserved in liquid media to avoid desiccation, preserve soft tissues and related microstructures (*i.e.*, scales in insects). Soft tissues preserved on these specimens are usually studied by sampling small regions (*i.e.*, destructive sampling). Studying only small samples of soft tissues, however, can hinder the interpretation of the nature of soft tissues, limiting our understanding of the biology of ancient animals.

The aims of the study are threefold: (1) to critically assess the versatility of mobile-MA-XRF to analyze specimens preserved in different media; (2) to develop a protocol to acquire and process the data; (3) to analyze the element-soft tissue associations in a large number of fossil vertebrate specimens preserving evidence of multiple soft tissues (*i.e.*, eyespots, skin, fur, feathers and internal organs) and compare chemical signals across taxa. This study demonstrates the usefulness of mobile-MA-XRF analyses for those fossil specimens that can be difficult to analyze using SR-MA-XRF and benchtop μ-XRF scanners due to their large size and/or conservation conditions. Ultimately, our study provides a solid framework to apply mobile-MA-XRF to analyze fossils, including a robust protocol to process and interpret the data.

2. Experimental

2.1 Fossil specimens

All the fossils ($n = 9$) considered for the study are part of the fossil vertebrate collection of Messel (ME) of the Senckenberg Research Institute and Natural History Museum (SMF) Frankfurt, Germany. The selection of specimens focused on those with evidence of soft tissues as a dark-colored carbonaceous film and conserved in three different media: resin (solid), glycerine (liquid), and water (liquid). The specimens are as

follows (see also ESI, Table S1†): a frog conserved in glycerine (SMF-ME 11390A, *Eopelobates wagneri*; Anura), three birds preserved in resin and water (SMF-ME 11414A, *Pumiliornis tessellatus*; SMF-ME 1758A, *Primozygodactylus major*; SMF-ME 11797A and its counter-slab SMF-ME 11797B, Aves indet.; see also ESI, Figs. S2 and S6†), four mammals conserved in resin (SMF-ME 11412A, *Macrocranion tupaiodon*; SMF-ME 11295A, *Masillamys beegeri*; SMF-ME 1583A, *Macrocranion tupaiodon*; and SMF-ME 0758A, *Pholidocercus hassiacus*), and finally a lizard conserved in resin (SMF-ME 11097B, Squamata indet.; Reptilia). The fossils from Messel are recovered from the Middle Messel Formation "oil shales", which are black pelites consisting of up to 40% of water (by weight).[55] To avoid desiccation, fossils are stored in water until preparation. The fossil bird (SMF-ME 11797B) conserved in water was therefore as close as possible to its state when it was discovered and was used to conduct pilot tests on the impact of fossils conservation method on analyses.

2.2 Mobile-MA-XRF analyses

The instrument used for the imaging spectroscopy experiments on the fossil specimens is the Bruker M6 Jetstream mobile-MA-XRF scanner.[32] It consists of a measuring head equipped with a 30 W Rh-target micro-focus X-ray tube and a 30 mm^2 Silicon-Drift (SD) detector, mounted on a X, Y-motorized stage with a maximum travel range of 80 by 60 cm^2 ($h \times v$) and a minimum step size of 10 μm. The object to be scanned remains stationary and the measuring head is moved over its surface during a scan with dwell times per pixel down to <10 ms. The X-ray tube features a maximum voltage and current of 50 kV and 0.6 mA, respectively. Five filters installed in a motorized filter wheel placed between the X-ray source and the lenses entrance allow the user to modify the spectral range of primary X-ray radiation emitted from the X-ray tube. A polycapillary optic allows to achieve a beam size as small as *ca.* 40 μm, by adjusting the distance between the measuring head and the object being scanned.[32] This is achieved by moving the measuring head along the Z-motorized stage (maximum travel range of 7 cm) using the focal plane of the stronger magnifying camera mounted on the measuring head to find the respective working distance by obtaining a sharp image. Due to the divergence of the lens each working distance corresponds to a certain spot size of the X-ray beam. The camera can be set manually to different working distances in five steps, depending on the beam size desired by the experimenter (100 μm, 200 μm, 300 μm, 400 μm, 500 μm image resolution).[32] This configuration allows to quickly modulate the beam size of the instrument without the need to change the beam-defining optic.

A detailed and critical description of the method used to acquire and process the data is presented herewith. Due to the size and fragility of the specimens, the metal frame on which the measuring head of the instrument travels was tilted to horizontal position for top-down geometry measurements. In this way, the fossil specimens were horizontally placed below the scanner frame on top of a metal-free table, one after the other, for a total of nine individual scans on selected areas of interest. The fossils were positioned considering (a) the detector position in relation to the area of interest to be scanned in order to improve the solid angle of detection and minimize shadowing effects affecting image resolution (two detectors mounted, *e.g.* left and right can reduce the effects), and (b) a relative position that reduced the total numbers of lines to scan, improving the effective measurement time. The elemental maps final orientation (left/right rotation; vertical/horizontal flip) was corrected for in data post-processing. The fossil specimens embedded in resin required no special preparation procedure before the scans. However, the surface of the fossilized frog conserved in glycerine (SMF-ME 11390A) was partially freed of liquid, to reduce at minimum the amount of glycerine on top of the fossil surface in order to have the instrument measuring head as close as possible to the actual fossil. The estimated thickness of glycerine left on top of the fossil surface was of *ca.* 1 mm. Prior to each measurement, mosaic images of the whole surface of the specimen were acquired in order to define the scanned area. This step allowed us to visualize the best area to scan.

The step size used ranged from 100 μm to 300 μm (see Table 1 for the specific step size chosen for each fossil specimen). Although a smaller step size would have contributed to increase the image resolution of the smaller fossil structures, this comes at the expense of a longer measurement time. The shortest dwell time utilized was of 75 ms per pixel, in order to still assure the collection of enough counts for those elements present at the trace level.[32] Furthermore, the chosen pixel time influences the X–Y-motorized stages speed. Although the reported maximum stage speed of the instrument is of 100 mm s^{-1}, it was noted that the slight vibrations induced by the motorized stages at such pace may partially affect the final image resolution. The authors do not recommend reaching overall measuring times equivalent to *ca.* 3 days of scans,[28] in order to avoid any possible radiation-induced side effects due to long exposure and potential alterations to the surface of the sample.[25] A high voltage of 50 kV and an anode current of 600 μA were set for all the mobile-MA-XRF experiments. No filter was used for changing the spectral range of the primary X-ray radiation. Finally, for the beam spot size, due to the slight fossils surface irregularities, the focal plane was always achieved by obtaining a sharp image at the highest topographic feature, to avoid any chance of collision between the measuring head of the instrument and the fossil. In fact, obtaining a spot size in the order of 35/50 μm by moving the *Z*-axis stage *ca.* 4 mm closer to the sample, when at 100 μm position, could trigger the ultrasonic distance sensor for collision protection integrated in the Bruker M6 Jetstream, causing the measurement to stop.‡ Therefore, for all the measurements a beam size of 100 μm was chosen. Notably, the given M6 Jetstream spot sizes are indicative; in fact, for non-flat samples the spot size on the samples surface normally varies during the scan depending on the lens divergence and the distance of the samples from the instrument head. The usual measurement distance with the Bruker M6 Jetstream is ~10 mm.[56] Next to the step size, the

‡ Bruker Nano Analytics, personal communication, 2021.

Table 1 Overview of the mapping and acquisition analytical parameters used in the mobile-MA-XRF measurements of the fossil specimens

Specimen #	Mapped area (mm × mm)	Step size (μm)	Pixel time (ms per pixel)	Overall time	Taxon
SMF-ME 11390A	55.8 × 45.6	150	80	2 : 39 h	*Eopelobates wagneri*
SMF-ME 11414A	78 × 46.6	250	100	1 : 45 h	*Pumiliornis tessellatus*
SMF-ME 11097B	163 × 85.3	280	80	4 : 10 h	Squamata indet.
SMF-ME 11797A	132 × 84.5	150	100	14 : 25 h	Aves indet.
SMF-ME 11797B	29 × 34.2	250	80	26 min	Aves indet.
SMF-ME 11412A	51.7 × 59.8	200	100	2 : 23 h	*Macrocranion tupaiodon*
SMF-ME 11295A	148 × 69.3	150	110	14 : 31 h	*Masillamys beegeri*
SMF-ME 1758A	152 × 70.5	300	100	3 : 33 h	*Primozygodactylus major*
SMF-ME 1583A	118 × 55.9	100	75	14 : 25 h	*Macrocranion tupaiodon*
SMF-ME 0758A	115 × 79.1	150	120	14 : 07 h	*Pholidocercus hassiacus*

minimal beam dimensions contribute to the smallest structures that can still be imaged with sufficient resolution.[57] Ideally, the beam size is in the same range as the structures to be resolved. Furthermore, the atomic number (Z) of the elements of interest play a role in the choice of the correct beam spot size. For example, beam diameters of 50 μm and 100 μm were reported to be particularly suited for XRF imaging spectroscopy of high-Z elements and low-Z elements, respectively, of fossils at synchrotron facilities.[58]

An overview of the mapping and acquisition parameters set for the mobile-MA-XRF scans is given in Table 1.

2.3 Elemental distribution maps: spectral region-of-interest (ROI) integration approach

Mobile-MA-XRF imaging spectroscopy with the Bruker M6 Jetstream is performed with the Position Tagged Spectroscopy (PTS) mapping option of the instrument, also known as Spectral Mapping or HyperMap.[59] The complete spectroscopic information, one spectral dimension (for each measured location) and two lateral dimensions (x; y),[60] is collected and saved in a multidimensional data cube, also called hyperspectral data cube. Given the centimeter scale analysis with micrometer resolution, for the spectral dimension such a data cube usually has several hundreds to thousands of entries. This makes the manual inspection of a few hundreds of thousands of spectra manually impossible.[61] A sum spectrum of all individual pixel spectra is therefore usually employed for this data treatment exploration phase, which aims at the identification of all relevant chemical features in a particular data set. However, for the successive data evaluation step to be successful, those features need to be represented in the form of comprehensive elemental distribution images. The latter will aid the interpretation of the acquired data.[62]

The routine for obtaining such graphical representation,[60] also used by the proprietary Bruker M6 Jetstream software package[32] and other software,[28,63] is referred to as Region-Of-Interest (ROI) imaging. Here, the X-ray map of a particular element peak is obtained by integrating a proper spectral energy window fixed around the signal of interest.[35,61,64–66] The quick estimation of the intensity of a peak by ROI integration and the immediate visualization of elemental distributions explain the frequent use of this procedure during on- or off-line processing of XRF data (*e.g.*, in the M6 Jetstream software it is possible to monitor the scan progress during acquisition, since the data stream is constantly updated).[32,61,66] However, this simple approach implies that the intensity of a peak should be substantially larger than the sum of all interfering lines and the spectral background within the integrated spectral ROI, in order to produce reliable elemental images.[61,67] This is mostly the case for major elements on weak background, allowing to assume the integrated ROI intensity to be a good estimate of the net intensity of the peak.[65,66]

Nevertheless, especially because of the limited resolving power of SD detectors used for X-ray spectra measurement, interference and peak overlap are common between the characteristic element lines.[68,69] Also, ROI images will inevitably include artifacts due to a higher spectral background, or for elements with a lower relative intensity (*e.g.*, because of a limited excitation efficiency or a lower relative abundance).[70] Here, the background intensity below the minor peak can be of the same order or larger than the net peak intensity. Further, most of the ROI spectral windows are contaminated by the tailing of strong X-ray peaks at energies up to ~2 keV above the window itself.[65,66]

It is possible to attempt the integration of spectral energy windows on weaker element lines in order to avoid the source of interference and obtain clearer X-ray images for an element. Unfortunately, this procedure does not yield reliable results when all lines for an element suffer interference. In case of the existence of a minor overlap interference-free line, the ensuing elemental distribution images will still suffer from the low number of counts,[71] making it impossible to obtain accurate artifacts-free maps. Furthermore, although it is a common procedure to subtract a constant background value from images to increase the contrast, this often does not lead to a better representation of the spatial distribution of the element but rather to inaccurate and misleading results, especially for trace elements.[65,72]

It is also possible to try to correct the ROI generated images for peak overlaps during post-processing. In this regard, a common procedure, also adopted by the Bruker M6 Jetstream proprietary software,§[32,73] involves the manual subtraction of

§ "Intensity math Enhance mode" element display option.

ROI images. Nonetheless, often overlaps are of complex nature and such procedures require a high amount of user inputs, which results in images with artifacts[73] that due to their misleading character are often not reported.[61,65]

Therefore, particularly due to the frequent peak overlap occurring in energy-dispersive X-ray spectra recorded using a polychromatic X-ray tube[66] and the discontinuous spectral background shape *e.g.*, derived from the pronounced variation in mean atomic number of the compositionally heterogeneous fossil specimens investigated and the conservation medium, the spectral ROI integration approach could not be used to create the final elemental distribution images. It only found a limited use in the preparatory data treatment phase.

2.4 Full spectral deconvolution and fitting

In order to exploit the multi-elemental character of the technique,[68,74] the spectral data was fully deconvoluted using PyMca (Python multichannel analyzer) freeware[69] and accurate estimates of the net intensities, *i.e.* peak areas (deconvoluted counts) of the characteristic fluorescence lines in the spectrum obtained.[68,75] Through the separation of the spectral background and the net elemental signals lower detection limits were attained,[35] all elemental peaks properly accounted for, and spectral interferences interpreted.

In PyMca, for each mobile-MA-XRF hyperspectral data cube a mathematical model was built and the peak areas resulting from the fitting of all spectra individually were used to reconstruct the elemental distribution images (see ESI, supplementary text†). The fast Statistics-sensitive Non-linear Iterative Peak-clipping (SNIP) filter was used for the treatment of the spectral background.[76] Elemental distribution images were obtained *via* the Batch Fitting tool in PyMca software package (version 5.8.1, project page at **https://sourceforge.net/projects/pymca/**). The data processing was run on a laptop computer that has 4 cores/8 threads, max. frequency 3.9 GHz.

2.5 Deconvoluted peaks

As all open-beam mobile-MA-XRF spectrometers operating under ambient conditions, the M6 Jetstream is limited in the detection of light elements as the low-energy fluorescence is easily absorbed by air. The element detection begins from Al, $Z = 13$. To improve the detection of light elements, the instrument can be equipped with a software-controlled He flush system to drive out air from the detection path. This improves the detection limit of all elements below Ca and the signal quality in general, allowing detection down to Na, $Z = 11$. Such electronically controlled helium purge system for enhanced light element performance, however, was not available for the present study, which led to the detection of Ar present in the surrounding atmosphere (~0.93%).[64] The primary X-ray radiation does not get through air without interaction but undergoes scattering and excites the air to emit fluorescence radiation.[56] Surface irregularities present on the sample under examination inevitably influence the distance between the sample and detector, and the air gap consequently. It is worth mentioning that of the elements of the air only Ar possesses a sufficiently strong characteristic radiation and relative abundance for being detected.[56] Albeit Cl, $Z = 17$, is not a major constituent of air, its presence in the air is not uncommon. Both the Ar and Cl signals were included in the fitting model (see ESI, Fig. S2N and S12–S20†).

Employing a polycapillary optic for focusing the primary X-ray radiation down to the micrometer scale, limits the range of high-energy lines that can be efficiently excited. This is due to the low transmission efficiency of polycapillary lenses for the high energy components of the primary X-ray radiation. As a consequence, the M6 Jetstream instrument lacks sensitivity for the K-lines of elements heavier than Rh (20.2 keV), with excitation power decreasing with increased Z.[32,77] A notable example is the Ba-K lines (~32–36 keV), which are not excited to a level detectable by the instrument.[70] Thus, the absence of the overlap-free Ba-K_α peak is not a good indicator of the absence of Ba in fossilized specimens.[28] From the instrumental point of view, for sensitive detection of heavy elements, collimators can be used instead of polycapillary optic. However, the use of collimators comes at the expense of (a) a considerable loss in spatial resolution, and (b) a reduction of the excitation intensity proportional to the collimator's aperture size, which requires a slower scanning speed increasing the overall scanning time consequently.[37] Another solution is to detect heavy elements, such as Ba, by means of the L radiation upon resolution of its overlap with the Ti-K radiation during fitting (see Sections 2.3 and 2.4).

In total, the K and/or L peaks of 23 elements were fully deconvoluted and fitted; the elements are as follows: Si, P, S, Cl, Ar, K, Ca, Ti, Cr, Mn, Fe, Co, Ni, Cu, Zn, Br, Sr, Y, Zr, Nb, Rh, Sn, and Ba. The elemental distribution maps generated with the PyMca Batch Fitting tool (see Section 2.4) were post-processed within the freeware to aid their interpretation (see Fig. 1–6 and ESI, Fig. S2−S11†). In this respect, exporting the mobile-MA-XRF maps into an external software package would have meant to create image artifacts due to the compression of peak intensity to normal image file. Thus, the authors avoid performing specific image manipulation procedures in external software[28,71] but advise to perform such operations in preferably open-access dedicated computer programs,[60] to obtain enhanced image legibility, accentuating the relevant features as well. For example, in several elemental distributions one or more regions with very high counts were found. Consequently, by means of the automatic scaling initially performed by PyMca freeware, the pixels with a lower recorded signal resulted rather dark. This visualization artifact was also recently encountered by Schrøder *et al. e.g.*, in the Mn map of a fossil fish scanned with the benchtop μ-XRF Bruker M4 Tornado[28] spectrometer. We therefore manually adjusted the minimum and maximum relative intensity values to where the bulk of the image pixels is in order to show the information carried by a particular elemental map. PyMca offers the possibility to display elemental maps using the linear or logarithmic scales as well as to apply a gamma-correction of the grey value scale.[61] Although the logarithmic intensity scale is reported to be of value in the presence of hot spots in the data allowing to see finer details in it as well, it found no application in the present study. On the

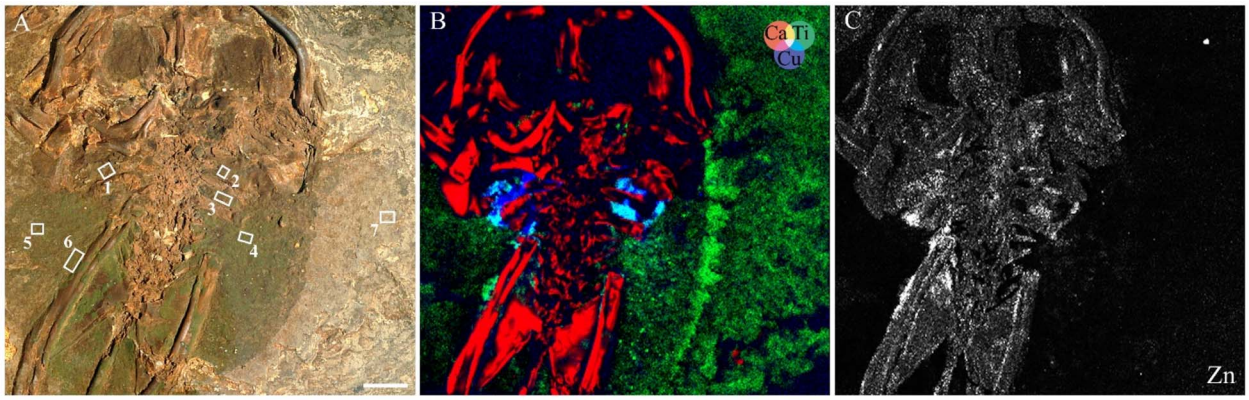

Fig. 1 (A) Optical image of *E. wagneri* (SMF-ME 11390A). (B) False color MA-XRF elemental images of Ca-K_α line (red), Ti-K_α line (green), and Cu-K lines (blue). (C) Zn-K lines elemental distribution. Numbered rectangles denote the regions of interest (ROIs). Scale bar represents 10 mm.

contrary, the gamma-correction was used to adjust the image contrast.

In all mobile-MA-XRF grayscale distribution images and false color maps presented in this work, the element relative abundance scales with the pixel brightness.[74]

2.6 PyMca ROI imaging tool image statistics plug-in

For the purpose of the statistical analysis for this work, a plug-in for image statistics was added to the RGB correlator of "PyMca ROI imaging tool"[78] by the software developers at the European Synchrotron Radiation Facility (ESRF), and made available to the users since PyMca version 5.8.1. It allowed to manually select areas on the stack of images from soft tissues and surrounding matrix for each fossil specimen and calculate the maximum and minimum pixel value of each element in the selected area, the number of selected pixels, and the mean and standard deviation of each element (see ESI, Fig. S21–S29 and Dataset S1†). Those values were then used in the statistical analysis.

2.7 Statistical analysis

The data available for this study is the averaged counts per each element in the selected areas, which limits the type of statistical analysis possible (see Sections 2.3, 2.4 and 4.4). Linear Discriminant Analysis (LDA) and analysis of variance were performed in R (RStudio Team, 2020, RStudio: Integrated Development for R. RStudio, PBC, Boston, MA **https://www.rstudio.com/**) as a preliminary statistical investigation of the data (see ESI, Datasets S2 and S3†). LDA is used to assess the presence of differences and similarities in the elemental chemistry among fossil specimens.[7] We used the counts data of 13 elements: Ca, Co, Cr, Cu, Fe, K, Mn, Ni, P, Sr, S, Ti, Zn to preliminarily assess differences in the metal composition of the regions of interest. We excluded from the analysis light elements (*e.g.*, Ar and Si), elements that consistently show counts below 1 in all regions of interest, and those elements that did not exhibit a clear association with the fossils. The first LDA analysis (using 13 elements) was performed by grouping the dataset by taxon as well as tissue types. A second LDA was performed using a reduced elemental dataset of 10 elements: Ca, Co, Cu, Fe, Mn, Ni, Sr, S, Ti, Zn, which are consistently associated with soft tissues in the fossils analyzed here. Analysis of variance is used to test whether the differences among groups are statistically significant. Normality and heterogeneity of variance (heteroscedasticity) were verified in R using residual plots. The datasets of single elements are almost all non-normal and heteroscedastic; thus, the analysis of variance was performed using the non-parametric Welch test and Games–Howell *post hoc* test. The dataset of Sr is normally distributed and heteroscedastic; thus, the Kruskal–Wallis and Dunn *post hoc* tests were used instead (see ESI, Dataset S3†).

3. Results

Mobile-MA-XRF analyses of individual fossil vertebrates reveal striking elemental distributions corresponding to anatomical features in almost all specimens analyzed. Cu consistently corresponds to regions in the torso/abdomen in almost all fossils analyzed; Zn (see ESI, Fig. S5J, S6I, S8K, S9J†), Ti and, to a lesser extent, S correspond to feathers and hair in birds and mammals. Ca is found associated with the skeletons and thus is not discussed further. Fe is the most abundant element in the sedimentary matrix, and it is usually associated with regions around the skeletal elements in fossils conserved in resin, which typically lack the original sedimentary matrix. Since fossil vertebrates are prepared using needles and not sandblast or other chemical methods of preparation, this signal is interpreted here as possible residue of sediment around the skeleton and it is not considered further here.

The frog conserved in glycerine, *E. wagneri* (SMF-ME 11390A, Fig. 1), shows a well-defined region enriched in Cu in the upper torso (Fig. 1B). The body outline is recognizable with the naked eye on the specimen as a green-colored film (Fig. 1A and ESI, Fig. S1D†) and a weak enrichment in Co is visible in the maps (see ESI, Fig. S3I†). The body outline is not enriched in any other element. The dark-colored eyespots (*i.e.*, within the orbit) are similar in elemental chemistry to that of the surrounding sediment.

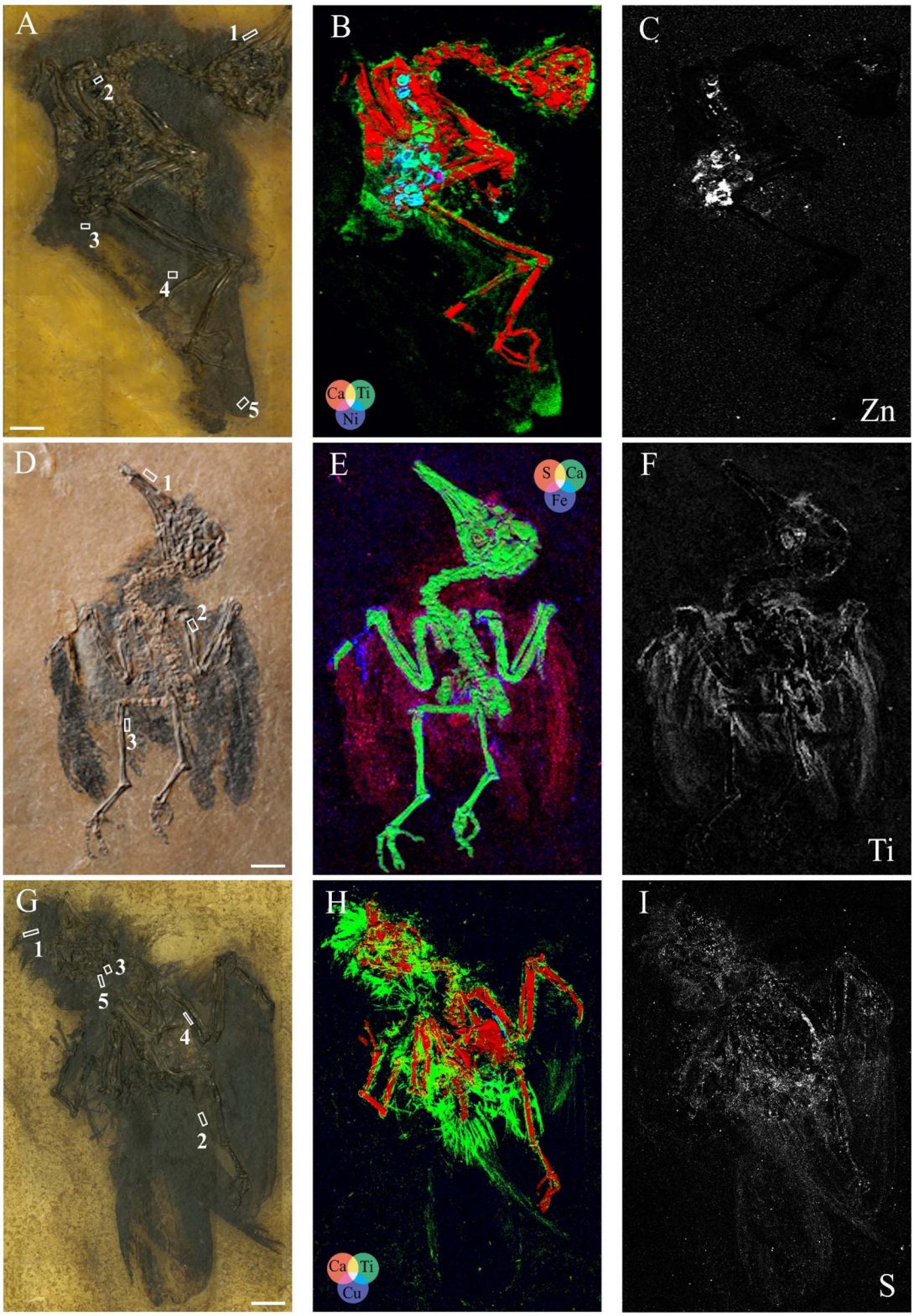

Fig. 2 (A) Optical image of *P. major* (SMF-ME 1758A). (B) False color MA-XRF elemental images of Ca-K_α line (red), Ti-K lines (green), and Ni-K lines (blue). (C) Zn-K lines elemental distribution. (D) Optical image of *P. tessellatus* (SMF-ME 11414A). (E) False color MA-XRF elemental images of S-K lines (red), Ca-K_α line (green), and Fe-K_α line (blue). (F) Ti-K lines elemental distribution. (G) Optical image of the indeterminate bird SMF-ME 11797A. (H) False color MA-XRF elemental images of Ca-K_α line (red), Ti-K lines (green), and Cu-K lines (blue). (I) S-K lines elemental distribution. Numbered rectangles in (A, D and G), denote the regions of interest (ROIs). Scale bars represent 10 mm.

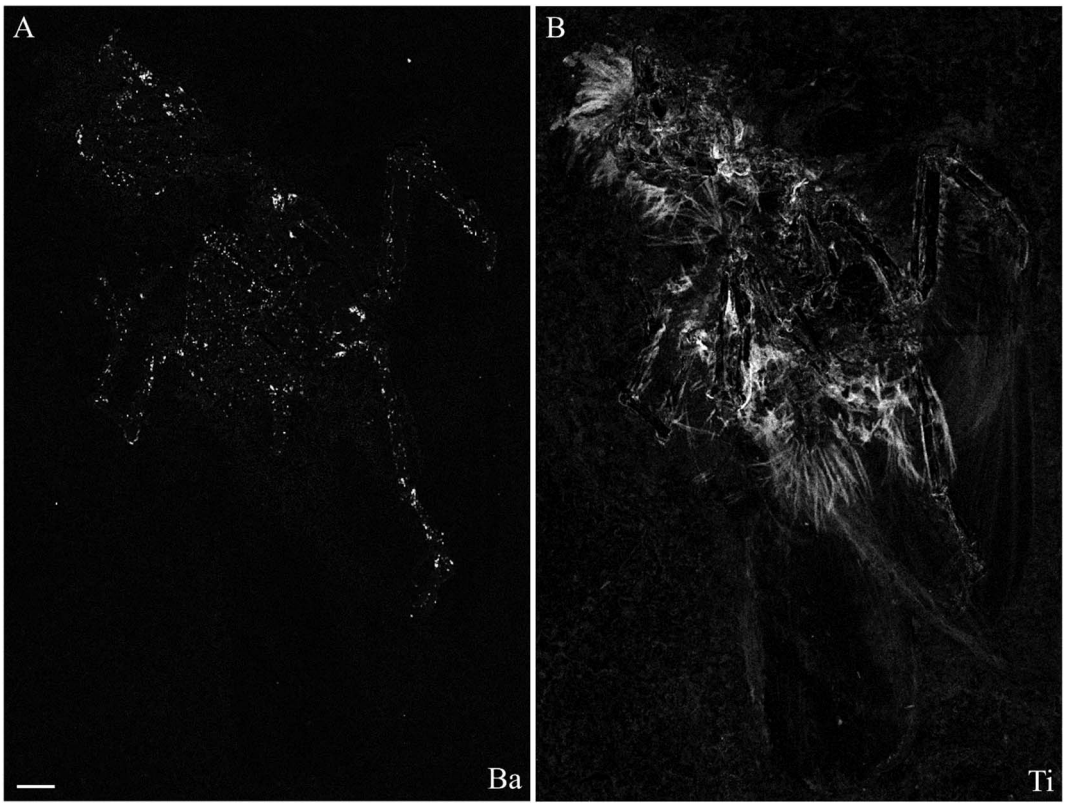

Fig. 3 Fossil bird SMF-ME 11797A. (A) Ba-L_3 line (includes L_α) MA-XRF elemental distribution image. (B) Ti-K lines MA-XRF elemental distribution image. Scale bar represents 10 mm.

The analysis of the bird specimens (SMF-ME 1758A, SMF-ME 11414A, SMF-ME 11797A; resin) reveals broad similarities between tissue types and elemental distributions. The feathers show an enrichment in Ti (Fig. 2B, F and 2H) and rarely, Cu. The spatial distribution of Ti and its association with the plumage is confirmed once the signal of Ba is deconvoluted showing a distinctive hot-spot like chemical signal (Fig. 3A and B). Cu is found associated with some of the feathers in specimen SMF-ME 11797A (Fig. 2H). Ni, and to a lesser extent Zn, are associated with the stomach content (*i.e.*, seeds) inside the abdomen (Fig. 2B and C).

The counterpart of specimen SMF-ME 11797A (called SMF-ME 11797B) was still conserved in its original sediment and was kept in water (*i.e.*, to avoid desiccation) at the time of our investigation. Both part and counterpart preserve roughly the same bones and soft tissue materials. Mobile-MA-XRF analysis yielded little signal for Fe (major element) associated with the sediment and Sr, Y and Zr (minor/trace heavy elements) associated with the bones (SMF-ME 11797B, see ESI, Fig. S2†).

In mammals (SMF-ME 11295A, SMF-ME 11412A, SMF-ME 1583A, SMF-ME 0758A; resin), the abdomen and thorax are associated with S, Ti, Zn and Cu (Fig. 4B, E, 4F, 5B and 5E). Integumentary structures are associated with S, Ti, Ni, and Cu (Fig. 4B, E, 4F, 5B, 5C and 5E). Stomach contents are associated with Ni, Cu, and Zn (Fig. 5C, E and 5F; see also ESI, Fig. S10†).

The analysis of the lizard specimen (SMF-ME 11097B; resin) reveals little of the soft tissue anatomy. The black-colored body outline is not enriched in any specific element (Fig. 6 and ESI, Fig. S1C†). Zn is associated with four small regions, three located in the abdomen and one in the tail. These regions do not exhibit a recognizable texture different from other areas of the specimen. Further investigation of the ultrastructure (*i.e.*, using SEM) is necessary to confirm the nature of the Zn-rich regions (that is, whether they represent preserved soft tissues or not). The presence of Ti and Fe is evident in regions around the skeleton (Fig. 6B) and represents possible residues of the original sedimentary matrix.

LDA of the fossil dataset reveals significant patterns in the data (Fig. 7). The LDA chemospace (LD1 = 52%; LD2 = 16%) of the data grouped by individual specimens shows a partial overlap between the mammal and bird specimens, which plot from the center to the left of the chemospace (Fig. 7A). This result suggests that the metal chemistry is similar among these taxa. The amphibian and reptilian specimens plot separately from the other two groups and from each other, respectively in the top and lower quadrants (Fig. 7A). Overall, the separation among the groups in the chemospace is controlled primarily by P, Cr, K and Co. These elements, except Co, however, are not associated with the soft tissues in the mobile-MA-XRF maps. The exclusion of P, Cr and K from the LDA analysis does not show better separation among taxa (Fig. 7B). The LDA chemospace (Fig. 7C and D; LD1 = 58%; LD2 = 29%) of the data grouped by tissue types reveals chemical differences among samples. Feathers plot near the center of the chemospace, mostly overlapping with the data from

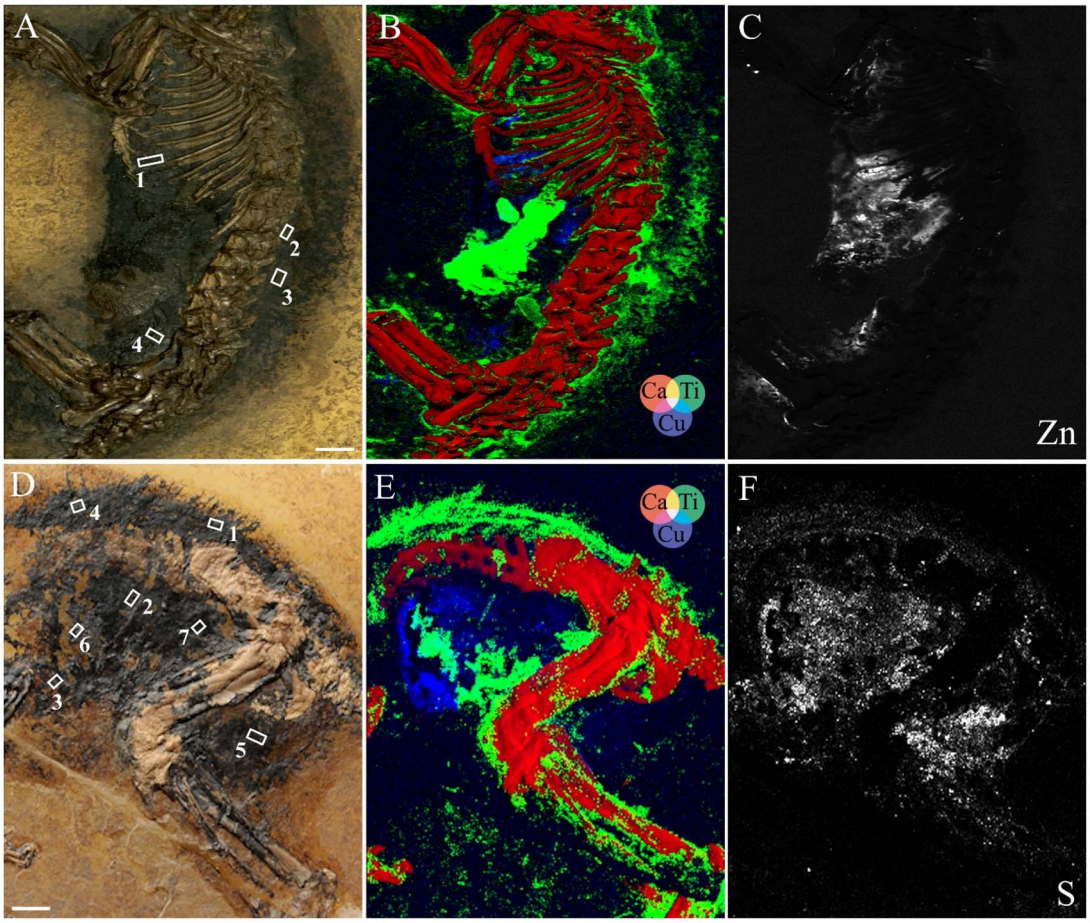

Fig. 4 (A) Optical image of *M. beegeri* (SMF-ME 11295A). (B) False color MA-XRF elemental images of Ca-K_α line (red), Ti-K lines (green), and Cu-K lines (blue). (C) Zn-K lines elemental distribution. (D) Optical image of *M. tupaiodon* (SMF-ME 11412A). (E) False color MA-XRF elemental images of Ca-K_α line (red), Ti-K_α line (green), and Cu-K lines (blue). (F) S-K lines elemental distribution. Numbered rectangles in (A and D) denote the regions of interest (ROIs). Scale bars represent 10 mm.

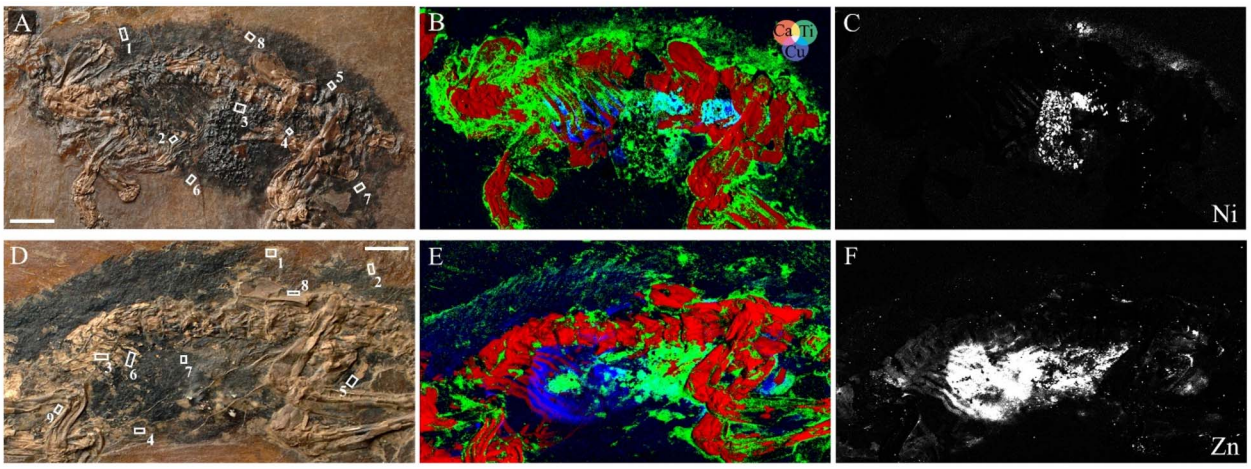

Fig. 5 (A) Optical image of *M. tupaiodon* (SMF-ME 1583A). (B) False color MA-XRF elemental images of Ca-K_α line (red), Ti-K lines (green), and Cu-K lines (blue). (C) Ni-K lines elemental distribution. (D) Optical image of *P. hassiacus* (SMF-ME 0758A). (E) False color MA-XRF elemental images of Ca-K_α line (red), Ti-K lines (green), and Cu-K lines (blue). Legend is not present as the elements are the same as Fig. 5B. (F) Zn-K lines elemental distribution. Numbered rectangles in (A and D) denote the regions of interest (ROIs). Scale bars represent 10 mm.

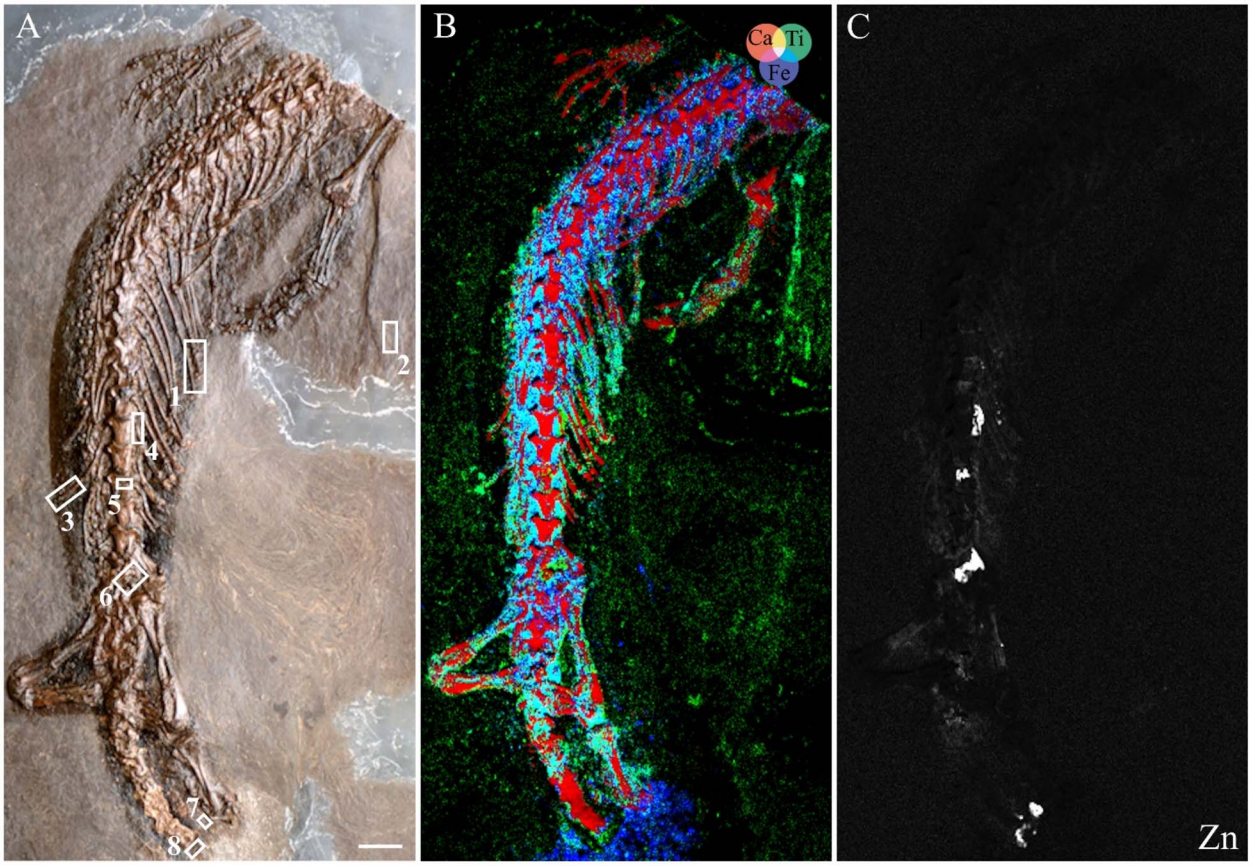

Fig. 6 (A) Optical image of the lizard (SMF-ME 11097B). (B) False color MA-XRF elemental images of Ca-K_α line (red), Ti-K lines (green), and Fe-K_α line (blue). (C) Zn-K lines elemental distribution. Numbered rectangles denote the regions of interest (ROIs). Scale bar represents 10 mm.

hair, which in turn extends from the center to the top half of the plot. Internal organs only slightly overlap with hair and feathers and occupy the center lower half of the chemospace. Skin regions plot separately from the other tissues on the right of the chemospace. The chemospace including the data from the elements associated with soft tissues in the mobile-MA-XRF maps (Fig. 7D) shows that feathers and hair are enriched in S and Ti compared to internal organs and skin; internal organs, in turn, are enriched in Cu, Ni and Sr compared to the other tissue types. Amphibian skin is enriched in Co, compared to the other tissues. Analysis of variance reveals that the chemical differences among tissues are statistically significant for all elements of interest, except Ti.

4. Discussion

Mobile-MA-XRF analyses revealed precise elemental spatial distributions associated with the Messel fossil vertebrates (see ESI, Table S1†). We found that the elements that are consistently associated with the soft tissues are S, Ti, Ni, Cu and Zn. Overall, this is similar to previous XRF studies,[7,15,17] including those that analyzed Messel specimens preserved exclusively in rock matrix, *i.e.*, without liquid media.[7,17] Furthermore, our LDA results show that statistically significant differences exist between the metal chemistry of fossil feathers, hair, amphibian skin and internal organs. Co is the primary discriminant for amphibian skin samples. Ni is associated with regions within the abdomen of some mammal and bird specimens; these regions preserve seeds and are thus interpreted as stomach contents.

The localization and well-defined distribution of key elements in the elemental maps allow for the interpretation of soft tissues in some of the fossils analyzed. Hair and stomach contents are typically associated with S and Zn, whereas feathers are typically enriched in Ti, S and Zn. In addition, in mammals (SMF-ME 11295A, SMF-ME 11412A, SMF-ME 1583A, SMF-ME 0758A), the presence of a Cu-rich region in the abdomen can be interpreted as the liver.[7] In *M. tupaiodon* (SMF-ME 1583A) the distributions of Ti and Cu coincide with the position of the kidneys in extant analogues (*i.e.*, small mammals). The presence of tissue-specific signals suggests that some of these associations are, at least in part, biological in origin.[7] Recent studies on extant and extinct taxa demonstrated that tissue specific elemental signatures exist in both modern and fossilized melanosomes[7] and thus it is plausible that the soft tissues elemental chemistry derives from preserved melanosomes in the taxa studied here.

Critically, elemental maps can be used to better visualize diverse soft tissues and/or areas for further micro-sampling and/or diagnostic analyses (*e.g.*, investigation of the quality of preservation of soft tissues microstructures, diagnostic chemical analysis to detect traces of biomolecules).

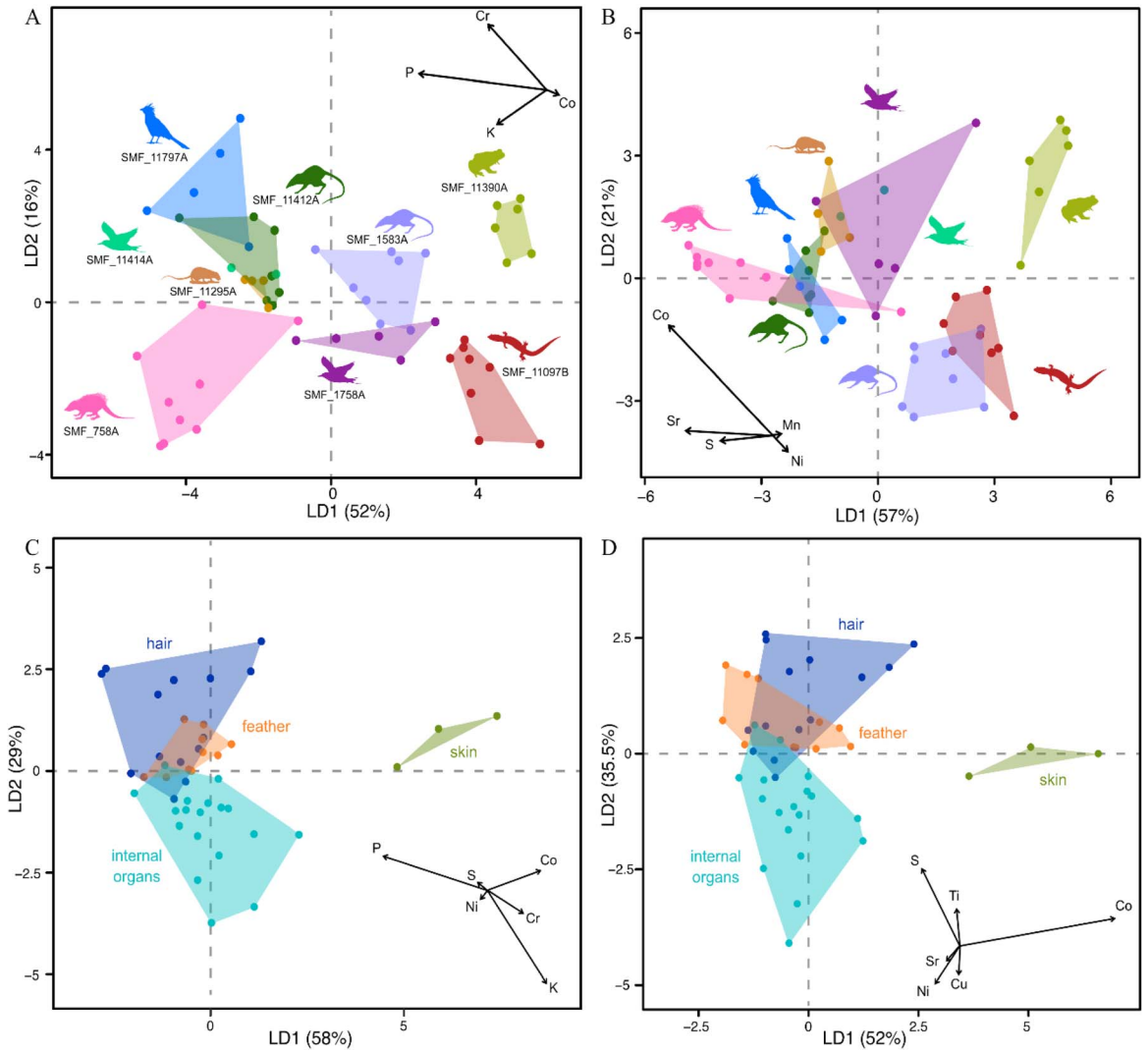

Fig. 7 Linear discriminant analysis (LDA) of mobile-macroscale scanning X-ray fluorescence (mobile-MA-XRF) imaging data of the Messel fossil vertebrates. Scatter plots of the LDA chemospace of the data arranged using single specimens as groups (A and B). LDA chemospace of the data arranged by tissue types (C and D). Biplots represent the contribution of each element (vectors) to the separation among groups. Only vectors that can be graphically represented in the figures are reported. Notes relating to the main text.

4.1 Comparison of mobile-MA-XRF with the M6 Jetstream relative to SR-MA-XRF and benchtop μ-XRF

Application of mobile-MA-XRF and benchtop μ-XRF spectrometry in paleontology has its advantages but is not without limitations. A critical discussion of this approach is included herewith. Until recently, sample sizes that could be analyzed using laboratory XRF scanners were limited by the chamber size of the analytical instrument, as in ref. 26–28. With the introduction of the M6 Jetstream it is possible to investigate large samples with scan areas of up to 800 mm × 600 mm in a single run.[32] In this work, the advantage of being able to scan from relatively small specimens (10 × 5 cm^2) to large specimens (>1 meter across) enabled the analyses of diverse taxa (see Table 1 and ESI, Table S1†). Fossil specimens of larger dimensions can be scanned in different sub-scans. However, if deemed necessary, the stitching of different fossil sub-scans together can be demanding, especially because of the difference in topography of the different areas selected and the possible resulting visible artifacts in the final stitched elemental distribution maps.[56,61,79] For that reason, future improvements in mobile-MA-XRF instrumentation should allow it to probe larger areas in one scan. Samples conserved in liquid media (*e.g.*, glycerin or water) could be scanned with mobile-MA-XRF. Here, the object to be analyzed is static and the X-ray tube and detector(s) installed on a motorized stage are moved in front of the object.[32] Conversely, in SR-MA-XRF[23] and benchtop μ-XRF the vertical and respectively horizontal travel stages on which the sample is placed, make it impossible to scan specimens in such conservation conditions. Mobile-MA-XRF is also free of the limit imposed by benchtop μ-XRF and most SR-MA-XRF instruments in terms of weight the sample stage can sustain. The M6 Jetstream open design and wheeled base for mobility allow complete flexibility in the alignment with the object. Specifically, the metal frame on which the instrument measuring head travels could be tilted

for sample analyses in horizontal position (top-down), contrary to the often-used vertical measurement orientation. The latter is impracticable for scanning specimens in liquid media. Mobile-MA-XRF experiments were performed at a relatively fast scanning pace, at high resolution, and with a user-friendly *in situ* experimental set-up (see Section 2.2 and Table 1).

4.2 Non-flat surface of fossil specimens

Large vertebrate fossils can display a relatively high degree of topographic variability due to the thick and irregular nature of the bones (three dimensional, that is, a volume), compared to soft tissue films (virtually two dimensional, that is, a plane).[57] Inherent surface irregularities are an issue for XRF mapping. A reasonably flat sample improves the spatial resolution of the measurement as an X-ray beam is typically broader below and above its focal plane, which results in larger beam spot sizes. A change of the distance between the instrument measuring head and the fossil surface (*i.e.* working distance) inevitably influences the measurement geometry,[56] and the sensitivity of the measurement in general.[56,80] Variations in the orientation of local fossil features relative to the primary X-rays change the relative intensity of XRF detected.[80,81] Potential solutions and improvements in instrumentation are (a) to enable mobile-MA-XRF to maintain the optimal distance between the object being scanned and the measuring head; (b) to use the M6 Jetstream new Aperture Management System (AMS). In particular, the latter technical feature enables to minimize the divergence of the beam and retain the measurement resolution over a certain range by increasing the depth of field. Consequently, the AMS achieves (a) a narrower beam, in order to keep the features in the sample in focus even below and above the analytical distance, (b) a longer working distance, which provides lower chance of collisions, and (c) smaller beam spot sizes for low-*Z* elements, enhancing their resolution. However, the AMS reduces the acceptance angle of the polycapillary optic, hence also the X-ray intensity, that is, the number of photons that reach the sample, is reduced. This explains the availability of the AMS with the dual 60 mm^2 SDDs M6 Jetstream only, as the reduction in intensity is partially cushioned by the increased solid angle of detection and signal processing capabilities of the 2 × 60 mm^2 SDDs. The AMS was not available for this work (see Section 2.2). A recent benchtop μ-XRF study of a fossil from inner Mongolia (China)[27] used a benchtop Bruker M4 Tornado Plus spectrometer, on which the AMS is mounted. However, the study does not report and/or comment neither on the specific usage of the system nor on the potential benefits for the methodological approach. In terms of data processing, the flattening of a particular map to the Compton image could be tested in order to reduce possible artifacts due to the non-flat regions in the specimen.[82]

4.3 Treatment of paleontological XRF imaging data

Appropriate data processing and analysis are also important aspects to consider prior to the application of XRF to analyze paleontological specimens. Two recent studies that used benchtop μ-XRF for this purpose,[27,28] did not provide data treatment procedures tailored to this new application which are, however, of importance to ensure the correct evaluation and interpretation of the acquired data. A lack of solid data processing methodologies can lead to a misidentification of the characteristic fluorescence peaks in the X-ray spectrum.[27,28] As reported previously (see Section 2.5), the high energy Ba-K lines (32–36 keV) are not excited to a detectable level when polycapillary lenses are used as beam-defining optic, such as in the M6 Jetstream instrument. Thus, the Ba elemental distribution needs to be based on the low energy L lines (4 keV). However, the Ba-L_α (4.46 keV) strongly overlaps with the Ti-K_α (4.51 keV) and the Ba-L_β (4.82 keV) with the Ti-K_β (4.93 keV). The impossibility to correctly deconvolute the Ba/Ti signals by means of the simple ROI integration approach (see Section 2.3), for instance due to the low relative intensity of the signals or the additional presence of the Cr-K_α tail/Cr-$K_{\alpha,\beta}$ lines in the spectrum, in order to obtain artifacts-free Ba-L images, was already reported in scanning experiments performed on an *Archaeopteryx* specimen *via* SR-MA-XRF[71] and for particle-induced X-ray emission (PIXE) spectroscopy[65] data. The Ba-L_3 line (includes L_α) distribution map of the fossil bird SMF-ME 11797A (see Section 3) shows the presence of the Ba signal in *hot spots* (Fig. 3A). On the one hand, the elemental map is free of noise and artifacts due to the Ti-K lines being ultimately not dominated by its distribution (Fig. 3B). On the other hand, the Ti distribution is real and not affected by the Ba-L lines (Fig. 3A and B). This example shows the capabilities of PyMca data analysis freeware, which, especially owing to the description of the different shells, permits the deconvolution of overlapped fluorescence lines.[69] Other noteworthy spectral overlaps,[35,71] namely the Mn-K_β/Fe-K_α and Co-K_α/Fe-K_β, were resolved following the same rationale (see Fig. 1–6 and ESI, Figs. S2–S20†). Results such as the detection of a Co signal possibly associated with the green-colored skin of the frog (SMF-ME 11390A), could be difficult to be achieved with the ROI integration approach (see Sections 2.3, 2.4, 2.5 and 3).

4.4 Statistical analysis performed with PyMca image statistics plug-in values

A limitation regards the restricted options to perform robust statistical analysis using the data that can be exported from PyMca software. In its current version (5.9.2), the image statistics plug-in allows only to calculate the mean and standard deviation per each element in the manually selected pixels (see ESI, Dataset S1†). At present, the counts of every element in each pixel of the selected area can be extracted only in the form of a single pixel selection, which, considering the presence of several hundreds of thousands of pixels in a scan commonplace, makes the use of that program functionality not possible. To perform statistical analysis, single pixel data should be exported (*i.e.*, raw pixel data[7,17]) and analyzed using standard multivariate statistical analysis, such as ANOVA and/or MANOVA and related *post hoc* tests. This is useful to statistically test differences in chemistry among the selected areas to support the interpretation of soft tissues. Nevertheless, preliminary statistical analysis can be performed using the averaged counts calculated for each selected area of all specimens analyzed. This allows us to draw broad conclusions on the distribution and relative abundance of the elements in the Messel fossil vertebrates analyzed (Fig. 7). Our

LDA shows an overlap in chemistry of the soft tissues between mammals and birds specimens when the data is plotted employing single specimens as groups (Fig. 7A and B). This might indicate similar diagenetic conditions during fossilization and/or an artifact of fossil preparation. The frog SMF-ME 11390A conserved in glycerine is found separated from the rest of the fossils conserved in resin (Fig. 7A and B). This might be due to the higher elemental mean values in the frog compared to the specimens in resin (see ESI, Fig. S21–S29 and Dataset S1†). A plausible explanation for the difference in counts is the presence of the sedimentary matrix in the case of the frog. We report low counts for all elements analyzed in specimens preserved in resin; this might be due to the very thin soft tissue material remaining after the preparation procedure.

4.5 Mobile-MA-XRF analyses of fossils conserved in glycerine and water

Our results show that conservation of fossil vertebrates in glycerine is not impacting on the elemental signal and the visualization of soft tissues. In the frog (*E. wagneri* SMF-ME 11390A, Fig. 1) it was detected a weak Co signal associated with the green-colored body outline and no distinct elemental association in the dark-colored eyespots (see Section 3). The lack of stronger elemental signal in these regions could be due to either a thicker layer of glycerine attenuating the characteristic XRF yields compared with that covering other body regions of the fossil, or the very thin layer of soft tissues preserved (<5 microns). Homogeneity of the XRF signal between melanosome-rich tissues and the sediment has been reported before[17] and might be due to the mobilization of elements during diagenesis, which can modify the original melanosome–metals association. A longer measurement scan and/or the reduction of the thickness of the glycerine layer might aid the identification of specific elemental signatures in those body regions. Nonetheless, our experiment shows that, assuring a sufficiently thin layer of glycerine on top of the fossil (see Section 2.2) for better surface exposure, specimens conserved in glycerine can be analyzed using our mobile-MA-XRF experimental setup and acquisition parameters (see Section 2 and Table 1). The bird specimen analyzed in water (SMF-ME 11797B, see ESI, Fig. S2†) showed no elemental signals of soft tissues and relatively low resolution in the elemental distribution maps. Since the specimen was still in its sedimentary matrix, a higher relative abundance of the elements than that found in the counter-slab specimen (SMF-ME 11797A) conserved in resin was expected (as in the frog SMF-ME 11390A). Due to the relatively thick layer of water on the surface of the specimen only the strongly attenuated signal from major elements or minor/trace heavy elements was detected. Further experiments are required to advance the analysis of fossils conserved in water – *e.g.*, scans of the same specimen under different water levels. In this regard, a mobile-MA-XRF setup allowing for faster scanning at the same time maintaining a correct pixel registration could enable measurements without nearly any water.

Without sampling the specimen, the absence of sedimentary matrix around the fossils hinders a straightforward distinction between fossil material and a possible sediment residue. However, the lack of sediment always provided sufficient elemental contrast between the fossil and the matrix under our experimental conditions.

4.6 Quantitative elemental analysis

An important aspect that needs significant method development is the elaboration of standard protocols for the quantification of the elemental concentrations present in the samples. Quantification analyses are routinely performed in studies using SR-MA-XRF,[7,58,71,83] often using different concentration units (*e.g.*, ppm or $\mu g\ cm^{-2}$). A study also compared XRF-based quantifications of trace elements (rare earth element, REE) to inductively coupled plasma-MS (ICP-MS) measurements on similar fossils from the same locality.[84] Quantitative measurements at ppm or $\mu g\ g^{-1}$ sensitivity at (sub)micron-scale spatial resolution, next to the generation of elemental maps, are likewise performed with PIXE (*e.g.*, to evaluate the chemical alteration of fossil bone).[85] Some of the challenges to obtain quantitative information from mobile-MA-XRF data on paleontological samples, were already reported.[29] These include the lack of suitable standards and the impossibility to detect very light elements. Further challenges may derive from (a) soft tissues are relatively thin which enhances the error due to depth heterogeneity; (b) low intensity signals are difficult to be quantified with confidence;[71] (c) variations in intensity because of the uneven surface of the fossils can hinder the variations due to elemental concentration (particularly for trace elements).[81] Developing a unified protocol for quantitative XRF analyses on element concentrations is necessary and will aid in comparative analyses of datasets available in the literature, strengthening our communal knowledge of biological and geological samples. Future collaborative efforts among experts and users are necessary to achieve this goal. Future versions¶ of PyMca software (or similar freeware) should include the possibility to automatically extract the counts/concentrations of each element present in each pixel of a selected area, in order to perform more advanced statistical analysis (see Sections 2.6, 2.7 and 4.4). Machine learning algorithms could be explored in order to enhance the XRF signal of specific structures in the elemental distribution maps,[24] aiding their interpretation. In the short-time frame, users should report detailed descriptions of their acquisition and data analysis strategies and publish the raw data (counts and/or concentrations) in the form of both spectra and tables to ensure reproducibility and consistency across studies and disciplines.

The full potential of the application of mobile-MA-XRF in paleontology has yet to be harnessed. The application of mobile-MA-XRF on fossil specimens is also expected to tackle research questions related but not limited to: the visualization and description of diverse soft tissues, the determination of the most suitable sampling locations, the assessment of the authenticity of fossil specimens (*e.g.*, to potentially expose forgeries[86,87]), and the detection of elements related to past restoration treatments

¶ V. A. Solé, personal communication, 2024.

on the fossil. Our study demonstrated the breadth of application of this technology to examine paleontological specimens preserved in various media and its usefulness in investigating the preservation of soft tissues in a non-destructive manner. We also report a detailed protocol to best perform data analysis which might aid measurement reproducibility ultimately unifying how experts use and report XRF data.

5. Conclusions

Our study shows that mobile-macroscale scanning X-ray fluorescence (mobile-MA-XRF) imaging spectroscopy provides precise two-dimensional laterally resolved elemental information from fossils preserved in solid resin and liquid glycerin. The data presented shows the importance of robust data analysis protocols in order to reach unambiguous interpretations. In this respect, the motivation behind the methodology chosen and details on its working principles and parameters used are provided to foster reproducibility and to give guidelines for the application of both mobile-MA-XRF scanners and benchtop μ-XRF scanners in paleontology. We also comment on crucial data acquisition process parameters providing user-oriented insights for the application of mobile-MA-XRF in paleontology. The details provided on the data processing steps taken on the ensuing elemental distribution maps serve to enhance their legibility. In this regard, image visualization artifacts that we and other working groups recently encountered are brought to light and concrete analytical solutions are proposed and explained. This study also proposes approaches to improve specific performances of mobile-MA-XRF, from the instrumentation point of view (for the detection of light elements, for the measurement of samples with an uneven surface, and for scanning areas larger than presently possible) and also from a data analysis standpoint (for detection of some heavy elements and for image resolution improvement or enhancement), which might be found applicable to other application fields as well. Future experimental work will focus (a) on the refinement of measurements of fossils in glycerine and especially in water; (b) on the implementation of quantification procedures to obtain the elemental concentrations within specific regions of the fossil specimens; (c) on the measurement of additional fossil samples from different fossiliferous deposits and preservation conditions.

Data availability

The data supporting this article have been included as part of the ESI† and Datasets.

Author contributions

MC, TL and VR conceptualized the project. MC curated the data. Formal analyses were performed by MC and VR. WE acquired the fundings. MC, TL and VR conducted the investigation. MC and VR developed the methodology. TL administered the project. TL and WE provided the resources. MC contributed to the software. TL, WE and VR supervised the project. VR contributed to the validation. MC and VR contributed to the visualization. MC and VR wrote the original draft of the published work. MC, TL, WE, and VR wrote, reviewed and edited the published work.

Conflicts of interest

There are no conflicts to declare.

Acknowledgements

The authors thank A. Vogel, M. Müller, K. Smith, S. Schaal, G. Mayr for their help with the fossil specimens. For the photos we thank A. Vogel. The authors thank Prof. J. Sander for support and M. Gerken for assistance during the analysis. B. Thybusch is acknowledged for the technical support during the project. The authors thank V. A. Solé for initiating the development of the software plug-in used in this work. R. Tagle from Bruker Nano GmbH, Berlin, Germany, is acknowledged for his help with the M6 Jetstream instrument. The authors thank S. Flege for the feedbacks provided during the revision of this manuscript. V. Rossi was supported by the Promotion of Educational Policies, University and Research Department of the Autonomous Province of Bolzano – South Tyrol within the research project "Living with the supervolcano – How Athesian eruptions destroyed and preserved 15 million years of Permian life" (nr. 11/34; CUP H32F20000010003) awarded to Prof. E. Kustatscher (Museum of Nature South Tyrol). V. Rossi is currently supported by an ERC consolidator grant "Palaeochem": H2020-ERC-COG-101003293 awarded to Prof. M. McNamara (University College Cork). The authors thank the Dr Rolf M. Schwiete Foundation for financial support.

References

1 R. Racicot, Fossil Secrets Revealed: X-Ray Ct Scanning And Applications In Paleontology, *Paleontol. Soc. Pap.*, 2016, **22**, 21–38.
2 J. A. Cunningham, I. A. Rahman, S. Lautenschlager, E. J. Rayfield and P. C. J. Donoghue, A virtual world of paleontology, *Trends Ecol. Evol.*, 2014, **29**, 347–357.
3 R. Georgiou, P. Gueriau, C. J. Sahle, S. Bernard, A. Mirone, R. Garrouste, U. Bergmann, J.-P. Rueff and L. Bertrand, Carbon speciation in organic fossils using 2D to 3D x-ray Raman multispectral imaging, *Sci. Adv.*, 2019, **5**, 1–9.
4 Y. Pan, L. Hu and T. Zhao, Applications of chemical imaging techniques in paleontology, *Natl. Sci. Rev.*, 2019, **6**, 1040–1053.
5 D. E. Briggs, The Role of Decay and Mineralization in the Preservation of Soft-Bodied Fossils, *Annu. Rev. Earth Planet. Sci.*, 2003, **31**, 275–301.
6 K. Glass, S. Ito, P. R. Wilby, T. Sota, A. Nakamura, C. R. Bowers, J. Vinther, S. Dutta, R. Summons, D. E. G. Briggs, K. Wakamatsu and J. D. Simon, Direct chemical evidence for eumelanin pigment from the Jurassic period, *Proc. Natl. Acad. Sci. U. S. A.*, 2012, **109**, 10218–10223.

7 V. Rossi, M. E. McNamara, S. M. Webb, S. Ito and K. Wakamatsu, Tissue-specific geometry and chemistry of modern and fossilized melanosomes reveal internal anatomy of extinct vertebrates, *Proc. Natl. Acad. Sci. U. S. A.*, 2019, **116**, 17880–17889.
8 P. L. Manning, N. P. Edwards, U. Bergmann, J. Anné, W. I. Sellers, A. van Veelen, D. Sokaras, V. M. Egerton, R. Alonso-Mori, K. Ignatyev, B. E. van Dongen, K. Wakamatsu, S. Ito, F. Knoll and R. A. Wogelius, Pheomelanin pigment remnants mapped in fossils of an extinct mammal, *Nat. Commun.*, 2019, **10**, 1–13.
9 T. S. Slater, S. Ito, K. Wakamatsu, F. Zhang, P. Sjövall, M. Jarenmark, J. Lindgren and M. E. McNamara, Taphonomic experiments reveal authentic molecular signals for fossil melanins and verify preservation of phaeomelanin in fossils, *Nat. Commun.*, 2023, **14**, 1–15.
10 M. H. Schweitzer, W. Zheng, A. E. Moyer, P. Sjövall and J. Lindgren, Preservation potential of keratin in deep time, *PLoS One*, 2018, **13**, 1–17.
11 T. S. Slater, N. P. Edwards, S. M. Webb, F. Zhang and M. E. McNamara, Preservation of corneous β-proteins in Mesozoic feathers, *Nat. Ecol. Evol.*, 2023, **7**, 1706–1713.
12 D. E. G. Briggs and R. E. Summons, Ancient biomolecules: their origins, fossilization, and role in revealing the history of life, *BioEssays*, 2014, **36**, 482–490.
13 L. A. Anderson, A chemical framework for the preservation of fossil vertebrate cells and soft tissues, *Earth-Sci. Rev.*, 2023, **240**, 1–17.
14 J. Wiemann, M. Fabbri, T.-R. Yang, K. Stein, P. M. Sander, M. A. Norell and D. E. G. Briggs, Fossilization transforms vertebrate hard tissue proteins into N-heterocyclic polymers, *Nat. Commun.*, 2018, **9**, 1–9.
15 R. A. Wogelius, P. L. Manning, H. E. Barden, N. P. Edwards, S. M. Webb, W. I. Sellers, K. G. Taylor, P. L. Larson, P. Dodson, H. You, L. Da-qing and U. Bergmann, Trace Metals as Biomarkers for Eumelanin Pigment in the Fossil Record, *Science*, 2011, **333**, 1622–1626.
16 N. P. Edwards, P. L. Manning, U. Bergmann, P. L. Larson, B. E. van Dongen, W. I. Sellers, S. M. Webb, D. Sokaras, R. Alonso-Mori, K. Ignatyev, H. E. Barden, A. van Veelen, J. Anné, V. M. Egerton and R. A. Wogelius, Leaf metallome preserved over 50 million years, *Metallomics*, 2014, **6**, 774–782.
17 V. Rossi, S. M. Webb and M. E. McNamara, Hierarchical biota-level and taxonomic controls on the chemistry of fossil melanosomes revealed using synchrotron X-ray fluorescence, *Sci. Rep.*, 2020, **10**, 1–10.
18 C. S. Rogers, T. I. Astrop, S. M. Webb, S. Ito, K. Wakamatsu and M. E. McNamara, Synchrotron X-ray absorption spectroscopy of melanosomes in vertebrates and cephalopods: implications for the affinity of Tullimonstrum, *Proc. R. Soc. Lond. B Biol. Sci.*, 2019, **286**, 1–8.
19 P. Gueriau and L. Bertrand, Deciphering Exceptional Preservation of Fossils Through Trace Elemental Imaging, *Microsc. Today*, 2015, **23**, 20–25.
20 V. Rossi, S. M. Webb and M. McNamara, Maturation experiments reveal bias in the chemistry of fossil melanosomes, *Geology*, 2021, **49**, 784–788.
21 C. S. Rogers, S. M. Webb and M. E. McNamara, Synchrotron x-ray fluorescence analysis reveals diagenetic alteration of fossil melanosome trace metal chemistry, *Palaeontology*, 2021, **64**, 63–73.
22 U. Bergmann, P. L. Manning and R. A. Wogelius, Chemical mapping of paleontological and archeological artifacts with synchrotron X-rays, *Annu. Rev. Anal. Chem.*, 2012, **5**, 361–389.
23 N. P. Edwards, S. M. Webb, C. M. Krest, D. van Campen, P. L. Manning, R. A. Wogelius and U. Bergmann, A new synchrotron rapid-scanning X-ray fluorescence (SRS-XRF) imaging station at SSRL beamline 6-2, *J. Synchrotron Radiat.*, 2018, **25**, 1565–1573.
24 N. P. Edwards, S. M. Webb and U. Bergmann, Photons, Folios, and Fossils: The X-ray Imaging and Spectroscopy Program of Ancient Materials at SSRL, *Synchrotron Radiat. News*, 2019, **32**, 22–28.
25 P. Gueriau, S. Bernard and L. Bertrand, Advanced Synchrotron Characterization of Paleontological Specimens, *Elements*, 2016, **12**, 45–50.
26 M. A. D. During, J. Smit, D. F. A. E. Voeten, C. Berruyer, P. Tafforeau, S. Sanchez, K. H. W. Stein, S. J. A. Verdegaal-Warmerdam and J. H. J. L. van der Lubbe, The Mesozoic terminated in boreal spring, *Nature*, 2022, **603**, 91–94.
27 Y. Chen, X. Li, F. Teng, J. Chen and R. R. Reisz, Micro-XRF Mapping Study On The Taphonomy Of A Jurassic Larval Salamander Fossil From Inner Mongolia Of China, *At. Spectrosc.*, 2023, **44**, 24–31.
28 A. E. Schrøder, D. K. P. Wielandt, J. A. Rasmussen, G. Carnevale and M. Storey, Benchtop micro–X-ray fluorescence, μXRF: an exciting tool for anatomical studies of fossil bony fishes, *Lethaia*, 2023, **56**, 1–29.
29 J. Li, R. Pei, F. Teng, H. Qiu, R. Tagle, Q. Yan, Q. Wang, X. Chu and X. Xu, Micro-XRF Study Of The Troodontid Dinosaur Jianianhualong Tengi Reveals New Biological And Taphonomical Signals, *At. Spectrosc.*, 2021, **42**, 1–11.
30 Bruker, Micro-XRF M4 Tornado, High Performance Micro-XRF Spectrometer, Brochure, 2024, M4-TORNADO-Brochure-EN-BRUKER.pdf.
31 Bruker, Micro-XRF M4 Tornado Plus, Super Light Element Micro-XRF Spectrometer. Brochure, 2024, M4-TORNADO-PLUS-Brochure-EN-BRUKER.pdf.
32 M. Alfeld, J. V. Pedroso, M. van Eikema Hommes, G. van der Snickt, G. Tauber, J. Blaas, M. Haschke, K. Erler, J. Dik and K. Janssens, A mobile instrument for in situ scanning macro-XRF investigation of historical paintings, *J. Anal. At. Spectrom.*, 2013, **28**, 760–767.
33 J. Dik, K. Janssens, G. van der Snickt, L. van der Loeff, K. Rickers and M. Cotte, Visualization of a lost painting by Vincent van Gogh using synchrotron radiation based X-ray fluorescence elemental mapping, *Anal. Chem.*, 2008, **80**, 6436–6442.
34 M. Alfeld, K. Janssens, J. Dik, W. de Nolf and G. van der Snickt, Optimization of mobile scanning macro-XRF systems for the in situ investigation of historical paintings, *J. Anal. At. Spectrom.*, 2011, **26**, 899–909.
35 M. Alfeld, PhD thesis, University of Antwerp, 2013.

36 F.-P. Hocquet, H. Del Calvo Castillo, A. Cervera Xicotencatl, C. Bourgeois, C. Oger, A. Marchal, M. Clar, S. Rakkaa, E. Micha and D. Strivay, Elemental 2D imaging of paintings with a mobile EDXRF system, *Anal. Bioanal. Chem.*, 2011, **399**, 3109–3116.

37 F. P. Romano, C. Caliri, P. Nicotra, S. Di Martino, L. Pappalardo, F. Rizzo and H. C. Santos, Real-time elemental imaging of large dimension paintings with a novel mobile macro X-ray fluorescence (MA-XRF) scanning technique, *J. Anal. At. Spectrom.*, 2017, **32**, 773–781.

38 G. van der Snickt, A. Martins, J. Delaney, K. Janssens, J. Zeibel, M. Duffy, C. McGlinchey, B. van Driel and J. Dik, Exploring a Hidden Painting Below the Surface of René Magritte's Le Portrait, *Appl. Spectrosc.*, 2016, **70**, 57–67.

39 M. Alfeld, W. de Nolf, S. Cagno, K. Appel, D. P. Siddons, A. Kuczewski, K. Janssens, J. Dik, K. Trentelman, M. Walton and A. Sartorius, Revealing hidden paint layers in oil paintings by means of scanning macro-XRF: a mock-up study based on Rembrandt's "An old man in military costume", *J. Anal. At. Spectrom.*, 2013, **28**, 40–51.

40 M. Alfeld, G. van der Snickt, F. Vanmeert, K. Janssens, J. Dik, K. Appel, L. van der Loeff, M. Chavannes, T. Meedendorp and E. Hendriks, Scanning XRF investigation of a Flower Still Life and its underlying composition from the collection of the Kröller–Müller Museum, *Appl. Phys. A: Mater. Sci. Process.*, 2013, **111**, 165–175.

41 G. van der Snickt, H. Dubois, J. Sanyova, S. Legrand, A. Coudray, C. Glaude, M. Postec, P. van Espen and K. Janssens, Large-Area Elemental Imaging Reveals Van Eyck's Original Paint Layers on the Ghent Altarpiece (1432), Rescoping Its Conservation Treatment, *Angew. Chem., Int. Ed.*, 2017, **56**, 4797–4801.

42 S. A. Centeno, C. Hale, F. Carò, A. Cesaratto, N. Shibayama, J. K. Delaney, K. A. Dooley, G. van der Snickt, K. Janssens and S. A. Stein, Van Gogh's Irises and Roses: the contribution of chemical analyses and imaging to the assessment of color changes in the red lake pigments, *Heritage Sci.*, 2017, **5**, 1–11.

43 K. Janssens, G. van der Snickt, M. Alfeld, P. Noble, A. van Loon, J. Delaney, D. Conover, J. Zeibel and J. Dik, Rembrandt's 'Saul and David' (c. 1652): Use of multiple types of smalt evidenced by means of non-destructive imaging, *Microchem. J.*, 2016, **126**, 515–523.

44 L. de Viguerie, P. Walter, E. Laval, B. Mottin and V. A. Solé, Revealing the sfumato technique of Leonardo da Vinci by X-ray fluorescence spectroscopy, *Angew. Chem., Int. Ed.*, 2010, **49**, 6125–6128.

45 N. de Keyser, G. van der Snickt, A. van Loon, S. Legrand, A. Wallert and K. Janssens, Jan Davidsz. de Heem (1606–1684): a technical examination of fruit and flower still lifes combining MA-XRF scanning, cross-section analysis and technical historical sources, *Heritage Sci.*, 2017, **5**, 1–13.

46 A. Harth, G. van der Snickt, O. Schalm, K. Janssens and G. Blanckaert, The young Van Dyck's fingerprint: a technical approach to assess the authenticity of a disputed painting, *Heritage Sci.*, 2017, **5**, 1–13.

47 G. van der Snickt, S. Legrand, J. Caen, F. Vanmeert, M. Alfeld and K. Janssens, Chemical imaging of stained-glass windows by means of macro X-ray fluorescence (MA-XRF) scanning, *Microchem. J.*, 2016, **124**, 615–622.

48 G. Magkanas, H. Bagán, M. C. Sistach and J. F. García, Illuminated manuscript analysis methodology using MA-XRF and NMF: Application on the Liber Feudorum Maior, *Microchem. J.*, 2021, **165**, 1–16.

49 P. Ricciardi, S. Legrand, G. Bertolotti and K. Janssens, Macro X-ray fluorescence (MA-XRF) scanning of illuminated manuscript fragments: potentialities and challenges, *Microchem. J.*, 2016, **124**, 785–791.

50 P. Ricciardi, K. A. Dooley, D. MacLennan, G. Bertolotti, F. Gabrieli, C. S. Patterson and J. K. Delaney, Use of standard analytical tools to detect small amounts of smalt in the presence of ultramarine as observed in 15th-century Venetian illuminated manuscripts, *Heritage Sci.*, 2022, **10**, 1–18.

51 M. Bicchieri, P. Biocca, C. Caliri and F. P. Romano, New discoveries on Leonardo da Vinci drawings, *Microchem. J.*, 2020, **157**, 1–6.

52 M. Bicchieri, P. Biocca, C. Caliri and F. P. Romano, Complementary MA-XRF and μ-Raman results on two Leonardo da Vinci drawings, *X-Ray Spectrom.*, 2021, **50**, 401–409.

53 S. Kaboth-Bahr, C. Schmitt, T. Bauersachs, C. Zeeden, T. Wonik, J. Schandl, O. Lenz, S. Wedmann, I. Vasiliev, A. Mulch, L. Lourens, J. Pross and A. Bahr, Improved chronostratigraphy for the Messel Formation (Hesse, Germany) provides insight into early to middle Eocene climate variability, *Newsl. Stratigr.*, 2024, **57**, 153–170.

54 F. Babarović, M. N. Puttick, M. Zaher, E. Learmonth, E.-J. Gallimore, F. M. Smithwick, G. Mayr and J. Vinther, Characterization of melanosomes involved in the production of non-iridescent structural feather colours and their detection in the fossil record, *J. R. Soc. Interface*, 2019, **16**, 1–9.

55 G. N. Büchel and S. F. K. Schaal, in *MESSEL - an Ancient Greenhouse Ecosystem*, ed. K. T. Smith, S. F. K. Schaal and J. Habersetzer, Schweizerbart Science Publishers, Stuttgart, Germany, 1st edn, 2018, pp. 7–15.

56 M. Alfeld, V. Gonzalez and A. van Loon, Data intrinsic correction for working distance variations in MA-XRF of historical paintings based on the Ar signal, *X Ray Spectrom.*, 2020, **50**, 351–357.

57 A. Knijnenberg, A. van Loon, J. Dik and A. van Asten, in *Leading Edge Techniques in Forensic Trace Evidence Analysis*, ed. R. D. Blackledge, Wiley, Hoboken, New Jersey, USA, 1st edn, 2022, pp. 213–244.

58 J. Anné, N. P. Edwards, R. A. Wogelius, A. R. Tumarkin-Deratzian, W. I. Sellers, A. van Veelen, U. Bergmann, D. Sokaras, R. Alonso-Mori, K. Ignatyev, V. M. Egerton and P. L. Manning, Synchrotron imaging reveals bone healing and remodelling strategies in extinct and extant vertebrates, *J. R. Soc. Interface*, 2014, **11**, 1–10.

59 M. Haschke, *Laboratory Micro-X-Ray Fluorescence Spectroscopy. Instrumentation and Applications*, Springer International Publishing, Cham, Switzerland, 1st edn, 2014.

60 I. Allegretta, S. Legrand, M. Alfeld, C. E. Gattullo, C. Porfido, M. Spagnuolo, K. Janssens and R. Terzano, SEM-EDX hyperspectral data analysis for the study of soil aggregates, *Geoderma*, 2022, **406**, 1–10.

61 M. Alfeld and K. Janssens, Strategies for processing mega-pixel X-ray fluorescence hyperspectral data: a case study on a version of Caravaggio's painting Supper at Emmaus, *J. Anal. At. Spectrom.*, 2015, **30**, 777–789.

62 M. Alfeld, S. Pedetti, P. Martinez and P. Walter, Joint data treatment for Vis–NIR reflectance imaging spectroscopy and XRF imaging acquired in the Theban Necropolis in Egypt by data fusion and t-SNE, *C. R. Phys.*, 2018, **19**, 625–635.

63 M. Occhipinti, R. Alberti, T. Parsani, C. Dicorato, P. Tirelli, M. Gironda, A. Tocchio and T. Frizzi, IRIS : A novel integrated instrument for co-registered MA-XRF mapping and VNIR-SWIR hyperspectral imaging, *X-Ray Spectrom.*, 2023, 1–11.

64 G. Celeux, S. X. Cohen, A. Grimaud and P. Gueriau, Hierarchical Clustering of Spectral Images with Spatial Constraints for the Rapid Processing of Large and Heterogeneous Data Sets, *SN Comput. Sci.*, 2022, **3**, 1–20.

65 C. G. Ryan, D. N. Jamieson, C. L. Churms and J. V. Pilcher, A new method for on-line true-elemental imaging using PIXE and the proton microprobe, *Nucl. Instrum. Methods Phys. Res., Sect. B*, 1995, **104**, 157–165.

66 K. Janssens, B. Vekemans, F. Adams, P. van Espen and P. Mutsaers, Accurate evaluation of μ-PIXE and μ-XRF spectral data through iterative least squares fitting, *Nucl. Instrum. Methods Phys. Res., Sect. B*, 1996, **109–110**, 179–185.

67 P. Gueriau, C. Mocuta, D. B. Dutheil, S. X. Cohen, D. Thiaudière, T. OT1 Consortium, S. Charbonnier, G. Clément and L. Bertrand, Trace elemental imaging of rare earth elements discriminates tissues at microscale in flat fossils, *PLoS One*, 2014, **9**, 1–9.

68 K. Janssens and P. van Espen, Evaluation of energy-dispersive x-ray spectra with the aid of expert systems, *Anal. Chim. Acta*, 1986, **191**, 169–180.

69 V. A. Solé, E. Papillon, M. Cotte, P. Walter and J. Susini, A multiplatform code for the analysis of energy-dispersive X-ray fluorescence spectra, *Spectrochim. Acta, Part B*, 2007, **62**, 63–68.

70 S. Flude, M. Haschke and M. Storey, Application of benchtop micro-XRF to geological materials, *Mineral. Mag.*, 2017, **81**, 923–948.

71 U. Bergmann, R. W. Morton, P. L. Manning, W. I. Sellers, S. Farrar, K. G. Huntley, R. A. Wogelius and P. Larson, Archaeopteryx feathers and bone chemistry fully revealed via synchrotron imaging, *Proc. Natl. Acad. Sci. U. S. A.*, 2010, **107**, 9060–9065.

72 P. van Espen, K. Janssens and J. Nobels, AXIL-PC, software for the analysis of complex X-ray spectra, *Chemom. Intell. Lab. Syst.*, 1986, **1**, 109–114.

73 S. Yan, J.-J. Huang, H. Verinaz-Jadan, N. Daly, C. Higgitt and P. L. Dragotti, A Fast Automatic Method for Deconvoluting Macro X-Ray Fluorescence Data Collected From Easel Paintings, *IEEE Trans. Comput. Imaging*, 2023, **9**, 649–664.

74 M. Colombo, F. Münch, P. Hoffmann, J. Sander and W. Ensinger, Scanning macro x-ray fluorescence spectroscopy maps for matching 17th century paintings color areas to different earth pigments uses and for investigating attribution issues, *X Ray Spectrom.*, 2024, **53**, 139–152.

75 P. van Espen and P. Lemberge, ED-XRF spectrum evaluation and quantitative analysis using multivariate and nonlinear techniques, *Adv. X-Ray Anal.*, 2000, **43**, 560–569.

76 C. G. Ryan, E. Clayton, W. L. Griffin, S. H. Sie and D. R. Cousens, SNIP, a statistics-sensitive background treatment for the quantitative analysis of PIXE spectra in geoscience applications, *Nucl. Instrum. Methods Phys. Res., Sect. B*, 1988, **34**, 396–402.

77 M. Alfeld, K. Mösl and I. Reiche, Sunset and moonshine: Variable blue and yellow pigments used by Caspar David Friedrich in different creative periods revealed by in situ XRF imaging, *X Ray Spectrom.*, 2020, **50**, 341–350.

78 M. Cotte, T. Fabris, G. Agostini, D. Motta Meira, L. de Viguerie and V. A. Solé, Watching Kinetic Studies as Chemical Maps Using Open-Source Software, *Anal. Chem.*, 2016, **88**, 6154–6160.

79 S. A. Barcellos Lins, B. Bremmers and G. E. Gigante, XISMuS — X-ray fluorescence imaging software for multiple samples, *SoftwareX*, 2020, **12**, 1–10.

80 E. C. Geil and R. E. Thorne, Correcting for surface topography in X-ray fluorescence imaging, *J. Synchrotron Radiat.*, 2014, **21**, 1358–1363.

81 D. M. Smilgies, J. A. Powers, D. H. Bilderback and R. E. Thorne, Dual-detector X-ray fluorescence imaging of ancient artifacts with surface relief, *J. Synchrotron Radiat.*, 2012, **19**, 547–550.

82 R. S. Popelka-Filcoff, C. E. Lenehan, E. Lombi, E. Donner, D. L. Howard, M. D. de Jonge, D. Paterson, K. Walshe and A. Pring, Novel application of X-ray fluorescence microscopy (XFM) for the non-destructive micro-elemental analysis of natural mineral pigments on Aboriginal Australian objects, *Analyst*, 2016, **141**, 3657–3667.

83 J. Anné, N. P. Edwards, A. van Veelen, V. M. Egerton, P. L. Manning, J. F. W. Mosselmans, S. Parry, W. I. Sellers, M. Buckley and R. A. Wogelius, Visualisation of developmental ossification using trace element mapping, *J. Anal. At. Spectrom.*, 2017, **32**, 967–974.

84 P. Gueriau, C. Mocuta and L. Bertrand, Cerium anomaly at microscale in fossils, *Anal. Chem.*, 2015, **87**, 8827–8836.

85 M. B. Goodwin, P. G. Grant, G. Bench and P. A. Holroyd, Elemental composition and diagenetic alteration of dinosaur bone: Distinguishing micron-scale spatial and compositional heterogeneity using PIXE, *Palaeogeogr. Palaeoclimatol. Palaeoecol.*, 2007, **253**, 458–476.

86 V. Rossi, M. Bernardi, M. Fornasiero, F. Nestola, R. Unitt, S. Castelli and E. Kustatscher, Forged soft tissues revealed in the oldest fossil reptile from the early Permian of the Alps, *Palaeontology*, 2024, **67**, 1–12.

87 S. Saverwyns, C. Currie and E. Lamas-Delgado, Macro X-ray fluorescence scanning (MA-XRF) as tool in the authentication of paintings, *Microchem. J.*, 2018, **137**, 139–147.